

©2015 IEEE. Personal use of this material is permitted. Permission from IEEE must be obtained for all other uses, in any current or future media, including reprinting/republishing this material for advertising or promotional purposes, creating new collective works, for resale or redistribution to servers or lists, or reuse of any copyrighted component of this work in other works.

<https://doi.org/10.1109/TIM.2015.2459472>

Identification and Control of a Cryogenic Current Comparator using Robust Control Theory

Marcos E. Bierzychudek, Ricardo S. Sánchez-Peña, and Alejandra Tonina

Abstract—This paper presents the model identification of a cryogenic current comparator (CCC). A dynamic model set is obtained and compared with experimental data in order to provide a realistic dynamical behavior of the system. To improve the performance of the CCC, an \mathcal{H}_∞ optimal controller is designed based on this model set. In this framework, a robust stability guarantee is provided and simulations of the closed-loop system illustrate the performance and robustness improvements.

Index Terms—Current comparator, \mathcal{H}_∞ control, metrology, resistance measurement, SQUID.

I. INTRODUCTION

THE outstanding sensitivity and accuracy of a cryogenic current comparator are based mainly on its superconducting inner shield and on the superconducting quantum interference device (SQUID). The shield provides negligible ratio errors, and the sensor can detect fractions of the magnetic flux quantum [1]. However, the SQUID has nonlinear dynamics and a limited slew rate. Hence, high frequency signals and noise can affect its performance or even impede the measurements. So a common guiding principle is to design the electronics, cables, screens, etc, with a focus on the best SQUID performance.

This work follows the same approach by applying robust control theory to the problem. The aim is to find a controller that improves the SQUID performance and allows faster current reversals. To this end, the feedback bandwidth must be equal to the working frequency range [2] in order to attenuate high frequency signals at the sensor input, including distortion created on current reversal. Traditional integral control is limited by the CCC self-resonant frequency [3], as Fig. 1 shows for a two-terminal CCC [4], thus a different control framework has to be applied.

In a previous work [5], the authors developed a theoretical model of a CCC and a \mathcal{H}_∞ controller design. In this article the model is adjusted using an identification procedure and validated by experimental data. The first step of this process is to obtain the parameters of the model, for example inductance and resistance, from data and/or specifications. Next, the initial model is adjusted with respect to several frequency responses

M. E. Bierzychudek is with the Centro de Física y Metrología, Instituto Nacional de Tecnología Industrial (INTI) and he is PhD student at the Instituto Tecnológico de Buenos Aires (ITBA), Bs. As., Argentina, e-mail: marcosb@inti.gob.ar.

R. Sánchez-Peña is with CONICET and ITBA, e-mail: rsanchez@itba.edu.ar.

A. Tonina is with the Centro de Física y Metrología, INTI, e-mail: atonina@inti.gob.ar.

Manuscript received April XX, XXXX; revised December XX, XXXX.

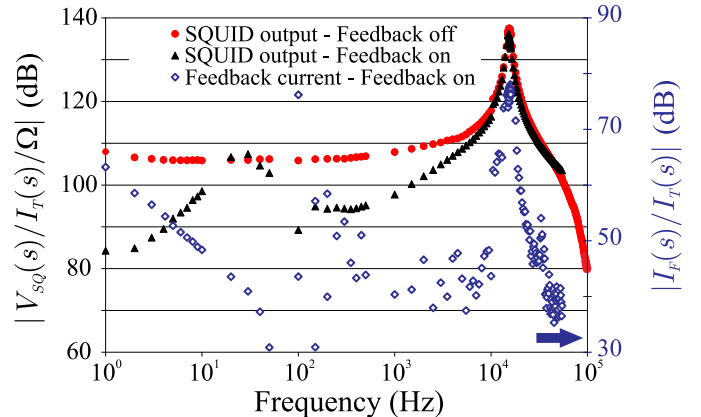


Fig. 1. Absolute value of the frequency response measurements of the SQUID voltage from a test current $I_T(s)$ in a single-turn winding, with integral feedback off (red circle) and on (black triangle). The response of the feedback current from the same input in closed-loop is shown in the secondary axis (blue diamond).

of the system measured with a lock-in amplifier in order to improve its fitting. A wider hypothesis is to represent the system by a set of models, instead of a single model, which considers a frequency dependent uncertainty bound. Here, the model set is compared and validated with measurements recorded by a digital oscilloscope. Then a controller is designed based on this dynamic set of models.

The CCC under study was designed to measure two-terminal high value resistors, scaling from the quantum Hall resistor or a 10 k Ω standard up to 1 G Ω [4], [6]. It has a single voltage source which allows a simple design and a unique ground reference, with no need of a voltage detector. In addition phosphor-bronze windings are used in order to damp the CCC resonance.

II. BACKGROUND: THEORETICAL MODEL

In [5], a theoretical model of a two-terminal CCC was obtained from its electrical equivalent circuit. The dynamics of each part of the system were represented as the Laplace transform of an ordinary differential equation, i.e. a transfer function which depends on the Laplace variable 's'. As Fig. 2 shown, $T_{L_11}(s)$, $T_{L_12}(s)$, $T_{L_1F}(s)$ represent the transfer functions from currents $I_1(s)$, $I_2(s)$ and $I_F(s)$ to the current in the primary winding $I_{L_1}(s)$, so $T_{L_1i}(s) = I_{L_1}(s)/I_i(s)$ with $i = 1, 2, F$. This winding has the larger number of turns and the lower resonant frequency, according to the assumption stated in [5]. These dynamics were obtained applying the

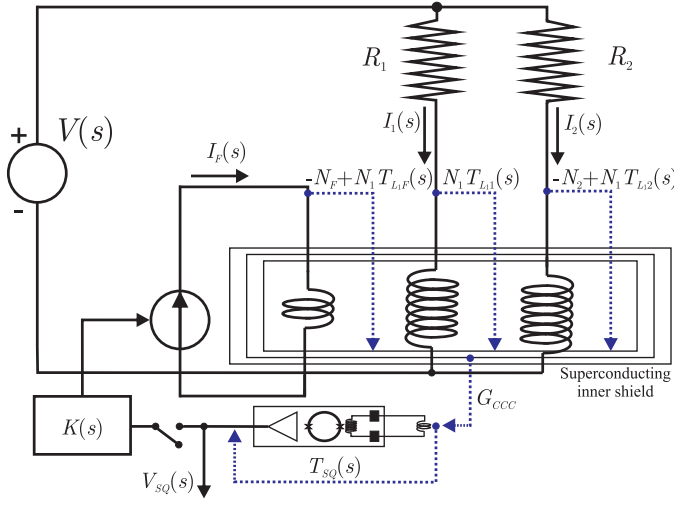


Fig. 2. Schematic diagram of the two-terminal CCC. The notation for the transfer functions from the origin to the end of the blue-dotted arrows is indicated. Table I presents the description of each symbol. In the feedback loop, a switch is included to indicate where the loop is opened.

superposition principle, and considering parasitic capacitance and resistance.

$$T_{L11}(s) = \frac{1}{C_1 L_1 s^2 + s \left(\frac{L_1}{R_1} + C_1 R_{W1} \right) + \left(\frac{R_{W1}}{R_1} + 1 \right)}, \quad (1)$$

$$T_{L12}(s) = \frac{M_{12} s \left(C_1 s + \frac{1}{R_1} \right)}{C_1 L_1 s^2 + s \left(\frac{L_1}{R_1} + C_1 R_{W1} \right) + \left(\frac{R_{W1}}{R_1} + 1 \right)}, \quad (2)$$

$$T_{L1F}(s) = \frac{M_{1F} s \left(C_1 s + \frac{1}{R_1} \right)}{C_1 L_1 s^2 + s \left(\frac{L_1}{R_1} + C_1 R_{W1} \right) + \left(\frac{R_{W1}}{R_1} + 1 \right)}. \quad (3)$$

The resistance R_1 is the standard resistor connected to the primary winding. L_1 , C_1 and R_{W1} are the inductance, stray capacitance and distributed resistance of the primary winding, respectively. M_{12} and M_{1F} are the mutual-inductances between the primary winding, and the secondary and feedback windings, respectively. The SQUID sensor in flux locked loop (FLL) mode is represented with a single pole transfer function, $T_{SQ}(s) = k_{SQ}/(1 + s/p)$, which has a DC gain k_{SQ} equal to the SQUID flux sensitivity. The SQUID output voltage, eq. (4), can be obtained applying Ampere's law to the CCC. Here N_1 , N_2 and N_F are the number of turns of the primary, secondary and feedback windings respectively, and G_{CCC} is the inverse of the linkage current. Table I defines all the symbols used in this document.

$$V_{SQ}(s) = T_{SQ}(s) G_{CCC} \cdot [I_1(s) T_{L11}(s) N_1 - I_2(s) (N_2 - T_{L12}(s) N_1) - I_F(s) (N_F - T_{L1F}(s) N_1)]. \quad (4)$$

The controller $K(s)$ measures the SQUID voltage and drives the feedback current, see Fig. 2. Therefore, currents $I_1(s)$ and $I_2(s)$ are outside the control loop. As a consequence, the terms $T_{L11}(s)N_1$ and $[N_2 - T_{L12}(s)N_1]$ do not have an effect on the closed-loop stability. Hence, this approach

TABLE I
SYMBOLS

Symbol	Description (unit)
C_1	Primary winding capacitance (F)
L_1	Primary winding inductance (H)
R_{W1}	Primary winding resistance (Ω)
M_{1i}	Mutual inductance between the primary winding and the winding i (H)
R_i	Resistor connected to the i winding (Ω)
N_i	Number of turns of winding i
p	SQUID cut-off radial frequency (rad/s)
k_{SQ}	SQUID flux sensitivity (V/Φ_0)
G_{CCC}	CCC amplification (Φ_0/AT)
s	Laplace variable
$j\omega$	Complex frequency variable
$I_i(s)$	Equivalent current source i (A)
$I_{L1}(s)$	Current in the primary winding (A)
$T_{L1i}(s)$	Transfer function from $I_i(s) \rightarrow I_{L1}(s)$ (A/A)
$T_{SQ}(s)$	SQUID transfer function (V/Φ_0)
$G_0(s)$	Nominal model from $I_F(s) \rightarrow V_{SQ}(s)$ (Ω)
$G(s)$	Model included in set Ψ (Ω)
$K(s)$	Controller transfer function (Ω^{-1})
$W_\Delta(s)$	Dynamic uncertainty weight
$V(s)$	Voltage source (V)
$V_{SQ}(s)$	Laplace transform of SQUID output (V)
Δ	Dynamic uncertainty
Ψ	Set of models
\mathcal{T}	Set of closed-loop models
$v_{SQ}(t)$	SQUID output (V)
$\hat{v}_{SQ}(t_q)$	Estimated SQUID output at time t_q (V)
\bar{v}_{SQ}	Mean value of SQUID output (V)
t	Continuum time variable (s)
T_s	Sampling period (s)
t_q	Sampling time (s)
q	Discrete time variable
F_I	Fit index

focuses on the transfer function from $I_F(s)$ to $V_{SQ}(s)$. Using the nominal values of the parameters the model is defined as follows:

$$G_0(s) = \frac{V_{SQ}(s)}{I_F(s)} = -T_{SQ}(s) G_{CCC} [N_F - T_{L1F}(s)N_1]. \quad (5)$$

It is assumed that the number of turns of the primary and feedback windings are fixed and have no uncertainty.

The linkage current of the current comparator, $1/G_{CCC}$, was measured and found to be consistent with data obtained three years earlier to within the measurement uncertainty (0.2%). Similar results were found for the flux sensitivity, k_{SQ} , but with 0.6% of uncertainty. In addition, the specification value of the SQUID cut-off frequency¹ was used [7].

The parameters in $T_{L1F}(s)$ were measured or calculated individually. R_{W1} was measured at 4.2 K using a high accuracy dc multimeter. Inductance L_1 was measured with a LCR meter, the resonant frequency was calculated as the average

¹At the SQUID design and assembly stage, this can be done by measuring the noise spectrum of the stand alone device, but this was not the case here.

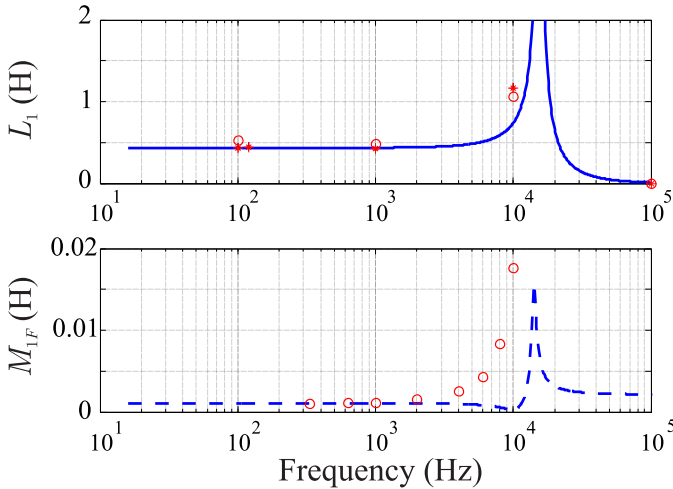


Fig. 3. Measurement results of L_1 and M_{1F} , in the upper and lower figures, respectively. The values at cryogenic (star) and ambient (circle) temperatures are shown. The simulations for the self-inductance at 4.2 K (blue solid line) and the mutual-inductance at 300 K (blue dashed line) are also presented.

of many resonant peak observations and from these results C_1 was obtained. The mutual inductance M_{1F} was determined by injecting a sinusoidal current in the feedback winding of one turn using a waveform generator and by measuring the voltage in the primary winding. The fast Fourier transform calculation of a digital oscilloscope was used to measure the amplitude of the desired frequency component. This measurement was performed at room temperature, and the self-inductance was measured also at 4.2 K, see Fig. 3. The resonant frequency of the coil with the greater number of turns (15.5 kHz) affects the measurements, for that reason the values at lowest frequencies were used in the initial model. The inductance of the feedback winding, not shown in the figure, presented a value of $2.6 \mu\text{H}$ at low frequencies. In addition, the effective self- and mutual- inductances were simulated. From equations (1) and (3) the effective value of these parameters were computed as $L_1 T_{L_1}(s)$ and $L_1 T_{L_1 F}(s) - M_{1F}$, respectively. In the case of the mutual-inductance, the simulation was performed by setting the parameters to values obtained at room temperature.

Similarly, other important parameters can be simulated, e.g. the leakage current in the primary winding when $I_1(s)$ is injected can be calculated as $[1 - T_{L_1}(s)] I_1(s)$. Previous works have obtained similar results with models based on the electrical equivalent of the CCC [8], [9] or performing estimations assuming bridge balance and superconducting winding [10], [11]. The advantage of the Laplace representation is that it can be evaluated at different conditions, e.g non-sinusoidal inputs. Furthermore, commercial programs are available to compute and improve the model [12].

To simplify the model identification, R_1 was set equal to $10 \text{ T}\Omega$, therefore it was disconnected. Note that equations (1) to (3) depend on R_1 , and it attenuates the resonance of the primary winding. In Fig. 4, a simulation of the transfer function in eq. (5) varying the resistance value of R_1 shows that the values larger than or equal to $10 \text{ M}\Omega$ generate negligible effects. On the other hand, a resistor of $1 \text{ M}\Omega$ or $100 \text{ k}\Omega$ connected to the primary winding strongly affects

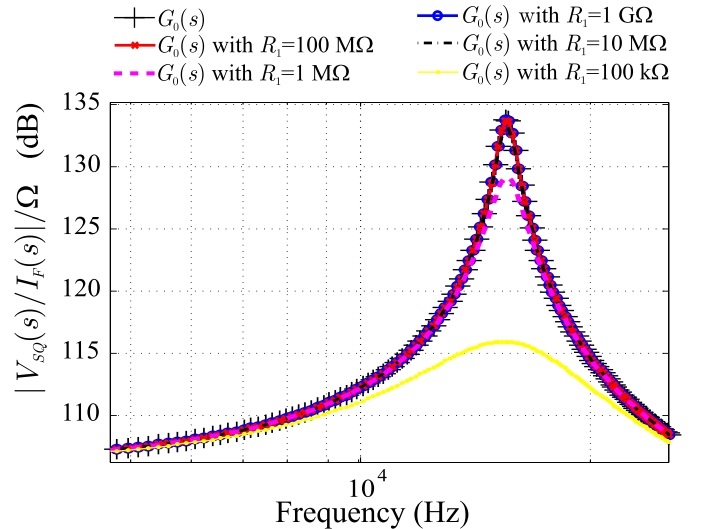


Fig. 4. Simulation of $G_0(s)$, eq. (5), with six values of R_1 . The transfer function for large value of resistance presents low deviations.

the transfer function. However, they are usually connected to windings with a low number of turns, producing a much lower attenuation. In this condition, the primary winding is in open circuit but the resonant frequency is damped due to the mutual inductance and stray capacitance arrangement of the CCC. This dynamics can not be explained with eq. (5). A complete model, that can include the effect of all the windings, resistors and other associated dynamics, will lead to high order equations and a more complicated controller. Therefore, a low order model is desirable but in the next section the model is expanded in order to include this behavior.

III. MODEL SET IDENTIFICATION

To improve the fitting of the theoretical model a *grey-box* identification was performed using an iterative prediction-error minimization method [12]. It minimizes a cost function, defined as the weighted quadratic norm of the prediction error vector $v_{SQ}(t) - \hat{v}_{SQ}(t)$, at $t = t_q$. Here $v_{SQ}(t_q)$ is the experimental data and $\hat{v}_{SQ}(t_q)$ is the estimated output at $t_q = q T_s$, $q \in \mathbb{Z}$ and T_s is the sample period. The experimental frequency responses were measured with a lock-in amplifier [13]. The test current in the single turn feedback winding was generated using a voltage-to-current amplifier connected to the voltage source of the lock-in amplifier. A computer program was used to control the instrument in order to sweep the input frequencies. It also modifies the input amplitude at each step to avoid jumps or saturation of the SQUID. For a given configuration, the SQUID output and the input current were measured, the latter as a voltage drop in a high quality metal film resistor connected in series. The magnitude of the transfer function was calculated as the ratio of the two measured values.

Fig. 5 shows the initial and the identified models, and the experimental data. All the curves agree on the resonant frequency and the DC gain. Note that the experimental data is always above the identified model and in some curves a small change can be found, which coincides with the modification

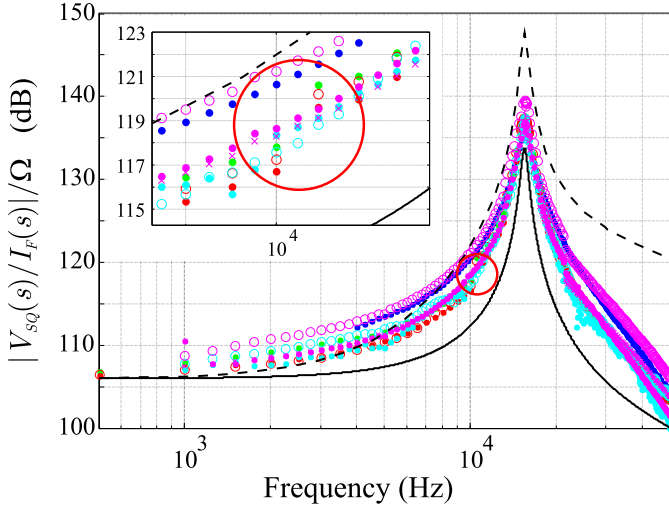


Fig. 5. Absolute value of the frequency response of the initial model (black dashed), identified model (black solid) and experimental data measured with a lock-in amplifier. Different colored lines distinguish the different measurement days.

TABLE II
INITIAL AND IDENTIFIED VALUES OF MODEL'S PARAMETERS.

Parameter	Initial value	Identified value
K_{SQ}	$0.779 \text{ V}/\Phi_0$	Fixed
G_{CCC}	$(3.91 \mu\text{AT}/\Phi_0)^{-1}$	Fixed
N_1	3100	Fixed
N_F	1	Fixed
R_{W1}	2850Ω	Fixed
p	314 krad/s	314 krad/s
C_1	242 pF	242 pF
L_1	0.434 H	0.434 H
M_{1F}	1.07 mH	0.22 mH
R_1	$10 \text{ T}\Omega$	$10 \text{ T}\Omega$

of the excitation amplitude (see the inset in the same figure). This may be produced by noise at the SQUID output or an excursion of the SQUID working point. The input amplitude was selected to maximize the signal-to-noise ratio, to maintain the FLL on, and to keep a low excursion of the working point.

In the optimization algorithm some parameters were fixed because their off-line measurements showed a good repeatability and confidence. These values are summarized in Table II, together with the initial and identified values of other parameters. Only the mutual inductance was clearly affected by the identification algorithm adjustment.

Differences between real and simulated frequency responses are generated by measurement errors, and unmodeled dynamics ([5], [14], [15]). Therefore, a more realistic description needs to include several models instead of a single one, in order to represent a physical system. Hence, in the robust control framework the system is described as a model set with its center in the nominal model previously obtained. The set of models that fully describes the CCC dynamic behavior is

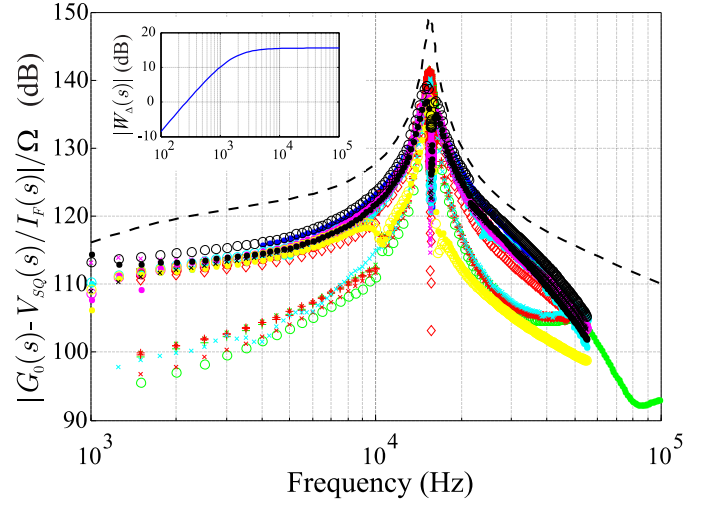


Fig. 6. Absolute value of the differences between nominal model and experimental data. The results are covered by the proposed dynamic uncertainty weight multiplied by the nominal model, $G_0(s) \cdot W_\Delta(s)$ (black dashed line). $W_\Delta(s)$ is shown in the inset figure.

defined as,

$$\Psi = \{G(s) = G_0(s) \cdot [1 + W_\Delta(s) \cdot \Delta], \Delta \in \mathbb{C}, |\Delta| \leq 1\}. \quad (6)$$

In this equation, $G(s)$ is a model included in the set, $G_0(s)$ is the identified nominal model, $W_\Delta(s)$ is the dynamic uncertainty weight and Δ is an unknown complex number included in an unitary bounded set. At a given frequency $s = j\omega$, all models included in the set belong to the circle of radius $|G_0(j\omega) \cdot W_\Delta(j\omega)|$ centered at $G_0(j\omega)$. In this framework, $|W_\Delta(j\omega)|$ represents the upper uncertainty bound of the model, as a function of frequency. If $|W_\Delta(j\omega)|$ is larger than one at a frequency ω , the nominal model differs more than 100% from the real system, so a “complete lack of knowledge” of the system prevents control above that frequency ([14], [15]). This is a practical result which indicates beforehand the maximum bandwidth that can be reached for this particular closed-loop controlled system.

To calculate the dynamic uncertainty weight, the nominal model was subtracted from the experimental data at each measured frequency and $W_\Delta(s)$ was adjusted to cover all these points. This is shown in Fig. 6 where the black dashed line is the proposed dynamic uncertainty weight multiplied by the nominal model, $G_0(s) \cdot W_\Delta(s)$. The weight $W_\Delta(s)$ is shown in the inset. It has a zero almost at the origin and a pole at $s = -10^4$ which produces a cutoff frequency of approximately 1.6 kHz. Notice that above 300 Hz, $|W_\Delta(j\omega)|$ is greater than unity (0 dB) and therefore limits the closed-loop bandwidth.

The experimental data was obtained by means of the lock-in amplifier and changing a setting and/or a parameter of the system, 33 frequency responses were evaluated. The purpose of these experiments was to represent different situations that may occur in practice and that should be “covered” by the model set Ψ . Time and liquid helium levels were the first variables to be analyzed. The measurements were performed during two weeks, while the He level varied between 43% and

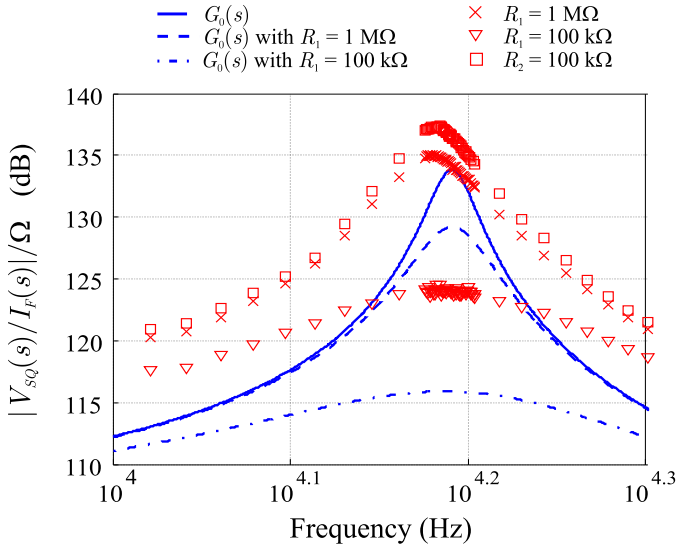


Fig. 7. Absolute value of the frequency response measurements (red) and simulation (blue) with a resistor connected. In the legend, the resistor and its position are indicated. The winding connected to R_1 has ten times more turns than the winding in series to R_2 .

10% with one refill. The results do not show any dependence on these variables.

Other measurements were performed with 100 k Ω and 1 M Ω value resistors connected in parallel to one of the CCC ratio windings, to simulate real and extreme measurement configurations. As Fig. 7 shows, the resistor connected in parallel changes the resonant peak and frequency. However, the frequency shift is not explained by the theoretical model. Since the CCC probe is not designed to have a resistor connected in parallel to the winding, the circuit must be closed through the system ground. This can increase the parallel capacitance and decrease the resonant frequency. In fact, elements with these resistance values are usually connected to windings with a low number of turns. In these configuration we found deviations of the measured frequency response from the nominal model within the repeatability of all the measured curves. Next, we extended the family of models to include uncommon and/or extreme settings in the set. To summarize, in the nominal model, primary resistor effects were neglected but they were included in the uncertainty weight. An alternative approach could be to make a model for each configuration, however this was not possible on the system due to the extra-capacitance problem, as it was explained at the beginning of this paragraph.

Finally, some measurements were performed with different input windings as i) two 1- turn windings and ii) one 2- turns winding. No significant variations were found within the measurement repeatability. The feedback winding is not usually changed in real measurements, however this experiment is useful to analyze the model. When the 2- turns feedback winding was used, the input current was multiplied by 2 in the calculations.

IV. EXPERIMENTAL VALIDATION

The family of models was compared with experimental data in order to evaluate the data fitting and coverage of the model

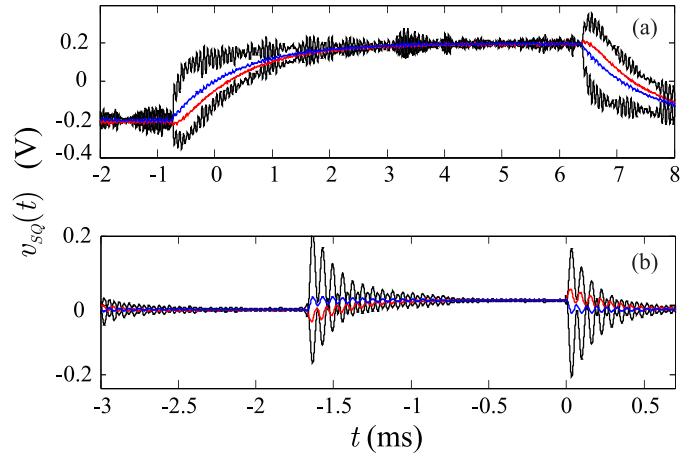


Fig. 8. Time response of the identified nominal model (blue) and the experimental (red) to a square wave input. Black lines represent two extreme models of the set: $G_{(\Delta=1)}$ and $G_{(\Delta=-1)}$. The systems with $\Delta = \pm 1$ amplify more the high frequency components in the recorder inputs, generating noisier outputs. Note that at 300 Hz the uncertainty weight is equal to the nominal system, see inset in Fig. 6, and the selection of Δ modified the gain of G .

set. Square, triangle, sinusoidal and impulse waveform current signals were supplied to the feedback winding. A digital oscilloscope was used to measure and save the input signals and the SQUID output voltages synchronously. The responses of the nominal model were simulated and compared against the recorded outputs. An index that indicates the percentage of the output that the model reproduces [12] was calculated as

$$F_I = 100 \cdot \left(1 - \frac{|v_{SQ}(t) - \hat{v}_{SQ}(t_q)|}{|v_{SQ}(t) - \bar{v}_{SQ}|} \right), \text{ with } t = t_q, \quad (7)$$

where \bar{v}_{SQ} is the mean value of $v_{SQ}(t)$. A perfect fit is represented with 100%, while 0% indicates that the model is equal to the mean value.

To this end, 34 measurements were performed with an average $F_I = 71\%$, 2/3 of these indexes were above this value. Two comparisons can be seen in Fig. 8 including the responses of two particular models in the set, $G_{(\Delta=\pm 1)} = G_0(s) \cdot [1 \pm W_{\Delta}(s)] \in \Psi$. From the first run (a) the nominal model output (blue) was quite similar to the real one (red) obtaining a fitting index better than 80%. This was not the case with the second simulation (b). Note that the two extreme models (black lines) “cover” the actual output. These experiments confirms that a model (or models) exists within the set that fits the measured data. As a consequence, a controller that stabilizes the model set will stabilize also the actual physical system.

V. CLOSED-LOOP SIMULATED RESULTS

Based on the previous model set, an \mathcal{H}_{∞} optimal controller was designed in order to provide closed-loop stability and performance to all models in the set (and hence the physical system). Here, performance is quantified as the attenuation of noise and disturbances at the SQUID input, and it is measured by the \mathcal{H}_{∞} norm of the closed-loop transfer function. A mixed sensitivity procedure was applied which balances the

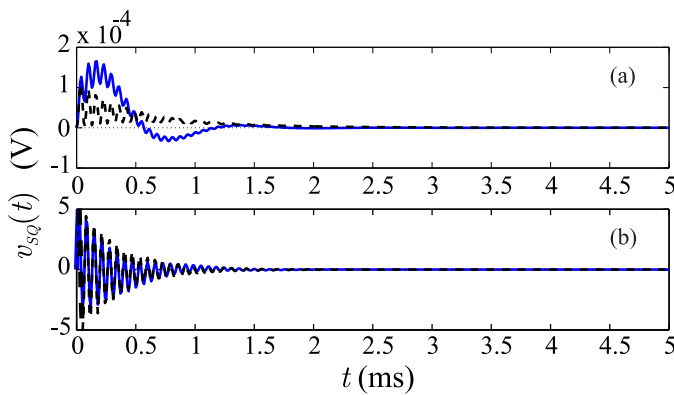


Fig. 9. Step (a) and impulse (b) simulated responses of the closed-loop system for the identified model (black dashed) and the worst case model (blue solid). The excitation amplitudes were 0.1 pA in the primary winding in both cases.

stability robustness and performance by means of uncertainty and performance weights ([14], [15], [16]). The controller behaves as an integrator from DC to 1.6 kHz, and at the resonant frequency its gain is sharply reduced and remained constant.

For a controller $K(s)$ connected to set Ψ , the set of all possible closed-loop transfer functions is as follows,

$$\mathcal{T} = \left\{ \frac{G_0(s) [1 + W_\Delta(s)\Delta]}{1 + G_0(s) [1 + W_\Delta(s)\Delta] K(s)}, \quad |\Delta| < 1 \right\}. \quad (8)$$

The stability of the whole model set is guaranteed when the denominator of the previous equation does not vanish for all $G(s) \in \Psi$ and s is in the complex positive semi-plane, i.e. $1 + G_0(s) [1 + W_\Delta(s)\Delta] K(s) \neq 0, \forall |\Delta| < 1, s \in \mathcal{C}^+$. It can be proved that a necessary and sufficient condition for controller $K(s)$ to stabilize all models in Ψ , defined as *robust stability*, is the following:

$$\left| \frac{G_0(s) \cdot K(s)}{1 + G_0(s) \cdot K(s)} W_\Delta(s) \right| < 1 \quad \forall s = j\omega. \quad (9)$$

In the present work this condition has been met. Fig. 9 illustrates this property, where the step and impulse responses of the nominal and worst case models ([14], [15], [16]) are represented, both being stable.

The performance of the \mathcal{H}_∞ and the integrative controller can be compared with the closed-loop transfer functions. The \mathcal{H}_∞ controller reduces the gain by 10 dB at the SQUID input up to 5 kHz. Since the design algorithm balances robust stability and performance condition, the model uncertainty strongly affects the performance. So, the uncertainty has to be considerably reduced. If the model uncertainty is minimized, the controller bandwidth can be increased until it attenuates the resonant peak without compromising the stability but this is difficult to achieve using traditional controllers.

VI. CONCLUSION

The CCC dynamic behavior was modeled by means of an identification procedure using experimental data, an agreement of at least 70% was obtained. Thus, the electrical equivalent of the comparator seems to be a good approximation. Its parameters can be measured independently and/or computed

from an identification process. A set of models was proposed to describe this system, and simulations showed that all the recorded data was included. This strengthens the assumptions made in [5] to construct the model, specially those that neglect the stray capacitance of the windings (except for the one with the largest number of turns). An \mathcal{H}_∞ controller was designed and robust stability for the model set was theoretically guaranteed and illustrated by closed-loop simulations.

Here, the SQUID working point excursions and output noise floor limited the repeatability of the frequency response measurements. This fact increased the uncertainty and $|W_\Delta(j\omega)|$, affecting the closed-loop performance. These two problems have opposite solutions, i.e. to reduce the noise effects a higher input signal is necessary, which can increment the working point excursion. A CCC with a lower resonant frequency and a larger SQUID bandwidth may accept a larger excitation input, increasing the signal-to-noise ratio. In this way, a smaller model uncertainty could be obtained and a faster controller could be designed.

ACKNOWLEDGMENT

The authors would like to thank to Martin Götz from PTB-Germany and Marcelo Cazabat from INTI-Argentina for many valuable discussions.

REFERENCES

- [1] J. M. Williams. Cryogenic current comparators and their application to electrical metrology. *IET Sci. Meas. Technol.*, 5(6):211–224, 2011.
- [2] D. Drung, M. Götz, E. Pesel, J-H Storm, C. Aßmann, M. Peters, and Th. Schurig. Improving the stability of cryogenic current comparator setups. *Supercond. Sci. Technol.*, 22, 2009.
- [3] K. Jones and M. D. Early. A quantum Hall cryogenic current comparator resistance bridge. In *Proc. CPEM Dig., Sydney, NSW, Australia*, pages 92–93. IEEE, 2000.
- [4] F. L. Hernandez-Marquez, M. E. Bierzychudek, G. R. Jones Jr., and R. E. Elmquist. Precision high-value resistance scaling with a two-terminal cryogenic current comparator. *Rev. Sci. Instrum.*, 85, 044701, 2014.
- [5] M. E. Bierzychudek, R. S. Sánchez-Peña, and A. Tonina. Robust control of a two-terminal cryogenic current comparator. *IEEE Trans. Instrum. Meas.*, 62(6):1736–1742, Jun. 2013.
- [6] R. E. Elmquist, E. Hourdakis, D. G. Jarrett, and N. M. Zimmerman. Direct resistance comparisons from the QHR to 100 M Ω using a cryogenic current comparator. *IEEE Trans. Instrum. Meas.*, 54(2):525–528, April 2005.
- [7] Quantum Design. *DC + RF SQUID Systems Brochure*. Available at: <http://www.qdusa.com/sitedocs/productBrochures/squid3.pdf>.
- [8] F. Renguez, O. Séron, L. Devoille, D. Placko, and F. Piquemal. A femto ampere current amplifier based on a 30 000:1 cryogenic current comparator. In *Proc. CPEM Dig., Rio de Janeiro, Brazil*, pages 296–297. IEEE, 2014.
- [9] K. Grohmann and D. Hechtfisher. Self-calibrating cryo current comparators for AC applications. *IEEE Trans. Instrum. Meas.*, 33(2):91–96, Jun. 1984.
- [10] F. Delahaye. An AC-bridge for low-frequency measurements of the quantized Hall resistance. *IEEE Trans. Instrum. Meas.*, 40(6):883–888, Dec. 1991.
- [11] H. Seppä and A. Satrapinski. AC resistance bridge based on the cyogenic current comparator. *IEEE Trans. Instrum. Meas.*, 46(2):463–466, April 1997.
- [12] L. Ljung. *System Identification ToolboxTM - User's Guide*. The MathWorks, 9.0 edition, March 2014.
- [13] T. B. Lawson, M. D. Early, and K. Jones. Simulation of a quantum hall cryogenic current comparator resistance bridge. In *Proc. CPEM Dig., Daejeon, Republic of Korea*, pages 623–624. IEEE, 2010.
- [14] K. Zhou, J. C. Doyle, and K. Glover. *Robust and Optimal Control*. Prentice-Hall, 1996.
- [15] R. S. Sánchez-Peña and Mario Sznaier. *Robust systems, Theory and Applications*. John Wiley & Sons, Inc, 1st edition, 1998.

- [16] G. J. Balas, J. C. Doyle, K. Glover, A. Packard, and R. Smith. *μ -Analysis and Synthesis Toolbox - User's Guide*. The MathWorks, 3.06 edition, June 2001.



Marcos Eduardo Bierzychudek received the electronics engineer degree from the Universidad de Buenos Aires, Argentina, in 2006. In 2005, he joined the Electricity Division, Instituto Nacional de Tecnología Industrial, Argentina, and he has worked since then in the Quantum Electrical Metrology Laboratory; involved in measurements of the Josephson effect and the Quantum Hall effect.



Ricardo S. Sánchez-Peña (StM86-M88-SM00) received the Electronic Engineer degree from the University of Buenos Aires (UBA, 1978), and the M.Sc. and Ph.D. from the California Institute of Technology (1986, 1988), both in Electrical Engineering. In Argentina he worked between 1977 and 2004 in CITEFA, CNEA and the space agencies CNIE and CONAE. He collaborated with NASA, the German (DLR) and Brazilian (CTA/INPE) space agencies. He was Full Professor at UBA (1989-2004), ICREA Senior Researcher at the UPC (2005-

2009, Barcelona) and visiting Prof./Researcher at several Universities in the USA and the EU. He has consulted for ZonaTech (USA), Alstom-Ecotecnia (Spain) and STI and VENG (Argentina). He published 3 books and more than 140 journal and conference papers. Since 2009 he is Director of the PhD Department at the Buenos Aires Institute of Technology (ITBA) and a CONICET Principal Investigator. He has applied Identification and Control techniques to practical problems in Engineering and Medicine.



Alejandra Tonina was born in Buenos Aires, Argentina. She received the Licenciatura and PhD degrees in Physics from the University of Buenos Aires, Buenos Aires, Argentina. She joined the National Institute of Industrial Technology (INTI), Argentina, in 1998. Her main responsibility is related to the maintenance of the electrical quantum standards. She is also involved in research work of QHE and new measurements techniques of the electrical magnitudes.